OPTICAL COHERENCE TOMOGRAPHY

Adolf F. Fercher
University of Vienna, Institute of Medical Physics, Währinger Straβe 13, A-1090 Wien, Austria
(Paper JBO-067R received December 27, 1995)

ABSTRACT

This paper gives an introduction to optical coherence tomography (OCT), explains its basic principles, and discusses the information content of OCT images. Various interferometric techniques used in OCT are reviewed and a short survey of results obtained so far in different fields of application and possible future developments are presented.

Keywords optical coherence tomography (OCT); low coherence interferometry (LCI); noise; tissues; waves.

1 INTRODUCTION

Tomography is based on the reconstruction of cross-sectional images of an object from its projections. While the basic mathematics was described as early as 1917 by J. Radon,[1] the implementation of this principle in medical imaging took a rather long time and led to a great number of configurations, depending on the properties of the various radiations used to generate the projections.[2] In the meantime, the term *tomography* is no longer restricted to image reconstruction from projections. It is also used whenever two-dimensional data are derived from a three-dimensional object to obtain a slice image of the internal structure. Depending on the radiation used, data acquisition is performed either by transmitted or reflected radiation. Three basic tomographic principles (Figure 1) can be used in optical transmission and reflection tomography: straight ray tomography, diffraction tomography, and time-resolved tomography.

At present, straight ray tomography is by far the most important and has been realized with a great variety of rays ranging from ultrasound to γ-rays. Time-resolved straight ray tomography [Fig. 1(c)] involves detecting and measuring the flight times of photons through the object to generate an image. This technique is still in a rather immature state.[3] Straight ray tomography, however, is a borderline case. It is a good approximation if diffraction and refraction can be neglected. In this case the filtered backprojection algorithm can be used to obtain cross-sectional images of the object.[4] If high-resolution images are required using optical radiation, diffraction and refraction become limiting factors and cannot be neglected.

Diffraction tomography [Fig. 1(b)] is part of the general problem of inverse scattering.[5] A basic mathematical theorem used to perform the reconstruction of the object structure is the Fourier diffraction theorem.[6,7] Much attention has also been paid to the development of further algorithms.[4,8] One-dimensional and two-dimensional optical reconstructions of cross-sectional images of an object were obtained from holographically recorded scattered field data nearly two decades ago.[9,10] These first attempts, however, were not further extended at that time because no spatially coherent broadband light sources were available. Later, with the availability of spatially coherent broadband light sources, diffraction tomographic principles were used to measure intraocular distance.[11]

In straight ray reflection tomography [Fig. 1(a)], transit times of the waves used or depth positions of reflecting sites in the object are measured. In diagnostic ultrasound, e.g., the waves propagate sufficiently slowly so that transit times can be measured with purely electronic means. In optics, specific techniques such as femtosecond impulses, photon density waves, and/or coherence techniques have to be used.[3] At present, in optical coherence tomography (OCT), the reflected straight ray approach is used and the object is scanned by the probing rays.

The first (*in vitro*) OCT images were presented by a group of researchers from Tufts University and Massachusetts Institute of Technology using a coherence domain reflectometer device based on low coherence interferometry (LCI).[12] The first *in vivo* tomogram (of the human optic disk) was published by our group[13] and was based on a dual beam LCI.[14–16] After initial studies,[17] the Boston group quickly presented studies on the clinical application of OCT in ophthalmic diagnostics,[18] in the examination of the anterior eye,[19] and the human retina,[20,21] and demonstrated the efficiency of this imaging technique in the quantitative evaluation and monitoring of various diseases of the macula and the optic nerve head.[22–26]

2 INFORMATION CONTENT OF OCT

In optics all approaches using straight rays, including the time-resolved techniques, neglect diffrac-

E-mail: adolf.friedrich.fercher@univie.ac.at

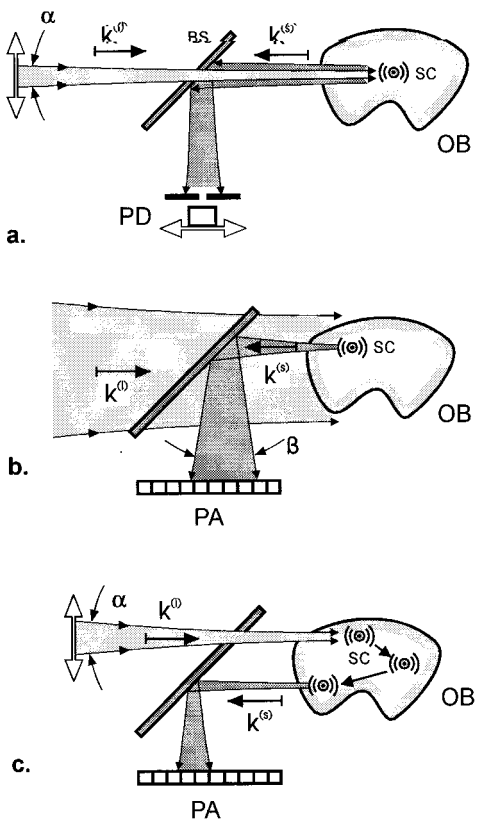

Fig. 1 Basic configurations of reflection tomography. Transversal resolution of these techniques is critically dependent on the aperture angles (α and β) of the light beam used. (a) Straight ray tomography needs depth location and lateral scanning (double arrow) to generate an image of the object; usually a single photodetector is moved synchronously with the beam. Depth resolution depends on transit time or path length resolution. (b) Diffraction tomography yields a diffraction pattern from which the object structure can be computed. Longitudinal resolution depends on the spectral width of the radiation used. (c) Time-resolved straight ray tomography yields a projection along various pathways through the object. Usually here, too, the illuminating beam laterally scans the object (double arrow). Again, depth resolution depends on transit time or path length resolution. OB, object; SC, scattering center; PD, photodetector; PA, photodetector array; BS, beam splitter.

tion. Hence these techniques are not sensitive to object structures comparable to a wavelength or smaller. In order to see what type of information can be obtained from optical tomography, we start with a short analysis of diffraction tomography,[4,6] use the Fourier diffraction theorem,[7] to discuss the available object data, and finally confine the treatment to backscattering (or reflected) straight ray tomography.

The basic physical situation is shown in Fig. 2, where the object is illuminated by a Gaussian light beam. Let the object be positioned at the beam waist and the object depth T be of the order of magnitude of the Rayleigh length of the light beam. Then we can assume the object is illuminated by an approximately plane wavefront $E^{(i)}$:

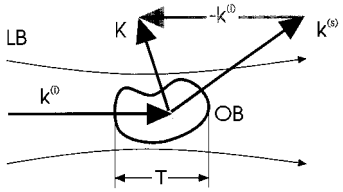

Fig. 2 Wave vectors in diffraction tomography. $\mathbf{k}^{(i)}$ is the wave vector of the illuminating Gaussian wave, $\mathbf{k}^{(s)}$ is the wave vector of the scattered wave, and $\mathbf{K}=\mathbf{k}^{(s)}-\mathbf{k}^{(i)}$ is the scattering vector. OB, object; LB, illuminating light beam; T, object depth.

$$E^{(i)}(\mathbf{r},\mathbf{k}^{(i)},t)=A^{(i)}\exp(i\mathbf{k}^{(i)}\mathbf{r}-i\omega t), \tag{1}$$

where $\mathbf{k}^{(i)}$ is the wave vector of the illuminating wave and $|\mathbf{k}^{(i)}|=k=(2\cdot\pi/\lambda)$ is the wave number. Let $E^{(s)}(\mathbf{r},\mathbf{k}^{(s)},t)$ be the scattered light wave. In 1969, Wolf[6] showed that within the accuracy of the first Born approximation, the three-dimensional distribution of the scattering potential $F(\mathbf{r})$ of the object can be computationally reconstructed from the distribution of amplitude and phase of the light scattered by the object. Wolf's solution for the scattered field is a volume integral extended over the illuminated object volume $V(\mathbf{r}')$:

$$E^{(s)}(\mathbf{r},\mathbf{k}^{(s)},t)=-\frac{1}{4\cdot\pi}\int_{V(\mathbf{r}')}F(\mathbf{r}')\cdot E^{(i)}(\mathbf{r}',\mathbf{k}^{(i)},t)\cdot G(|\mathbf{r}-\mathbf{r}'|)\cdot d^3\mathbf{r}', \tag{2}$$

with Green's function of the wave equation

$$G(|\mathbf{r}-\mathbf{r}'|)=\frac{\exp(i\cdot k^{(s)}\cdot|\mathbf{r}-\mathbf{r}'|)}{|\mathbf{r}-\mathbf{r}'|}$$

and the scattering potential

$$F(\mathbf{r})=-k^2\cdot[m^2(\mathbf{r})-1], \tag{3}$$

which determines the relative amplitudes of the scattered wavelets. $m=n+i\cdot\kappa$ is the complex refractive index of the object with n being the real part obeying the Lorentz-Lorenz equation and κ being the absorption coefficient.[27] In the past, mainly *in vitro* data on the refractive index of biological materials were collected.[28–35] Until very recently, only few data were available on refractive indices of *in vivo* human tissue obtained e.g., from low-coherence reflectometry[36] and Scheimpflug photography[37] (see also Secs. 5.1 and 5.2). In biological tissue the scattering potential mainly depends on the protein content:

$$m\cong n=n_s+\alpha\cdot C,$$

with n_s= refractive index of the solute, α = specific refractive increment of proteins [mostly approximately 0.0018 (100 ml/g)] and C= concentration. Hence basically the distribution of the refractive index or protein content contributes to the image. Furthermore it can be shown that far-field scattering is a reasonable approximation in LCI. Then the

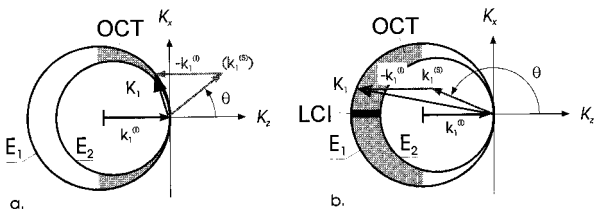

Fig. 3 Ewald sphere representation of backscattering in OCT. $\mathbf{E}_1$ and $\mathbf{E}_2$ are the Ewald spheres corresponding to wavelength λ_1 and λ_2 respectively. $\mathbf{k}_j^{(i)}$ and $\mathbf{k}_j^{(s)}$ are the wave vectors of illuminating and scattered waves with wavelength λ_j. $\mathbf{K}_j$ is the corresponding scattering vector. Using forward scattering (a) and backscattering (b) and a wavelength range from λ_1 to λ_2 gives access to Fourier data in the shadowed areas between the two corresponding Ewald spheres $\mathbf{E}_1$ and $\mathbf{E}_2$. LCI only gives access to Fourier data on the $\mathbf{K}_z$-axis.

scattered field is proportional to the Fourier transform of the scattering potential of the object:[11]

$$E^{(s)}(\mathbf{r},\mathbf{k}^{(s)},t) = -\frac{A^{(i)}}{4\cdot\pi\cdot D}\exp(i\cdot\mathbf{k}^{(s)}\cdot\mathbf{r} - i\cdot\omega\cdot t) \cdot \int_{V(\mathbf{r}')} F(\mathbf{r}')\cdot\exp(-i\cdot\mathbf{K}\cdot\mathbf{r}')\cdot d^3\mathbf{r}', \tag{4}$$

where the amplitude $A^{(i)}$ of the illuminating wave has been assumed constant within the object. D is a mean distance of the position $\mathbf{r}$ from the object. Hence the three-dimensional scattering potential $F(\mathbf{r})$ can be obtained from the scattered field $E^{(s)}(\mathbf{r},\mathbf{k}^{(s)})$ by an inverse Fourier transform. $\mathbf{K}=\mathbf{k}^{(s)}-\mathbf{k}^{(i)}$ is the scattering vector. For any direction of the scattered light, $\mathbf{K}$ points onto the surface of a sphere. This is the Ewald sphere, well known in crystallography.[38,39] The Ewald sphere can be used to further discuss the relation between scattering and available Fourier data as shown in more detail in Figure 3.

To obtain a true three-dimensional reconstruction of the scattering potential F, a certain range of data $E^{(s)}$ in the three-dimensional Fourier space has to be measured. However, as can be seen from Fig. 3, only a rather limited section of the Fourier data of the object can be obtained from scattered light data. Using one particular wavelength, we have access to Fourier data only on the surface of the corresponding Ewald sphere. These data are basically two-dimensional. Additional wavelengths have to be used in order to get access to a true three-dimensional Fourier data set. Forward scattering and a wavelength range from λ_1 to λ_2, for example, gives access to Fourier data in the shaded volume indicated in Fig. 3(a). Using forward scattering limited to θ=0 would only give access to the Fourier datum at the origin. Hence, according to Fourier theory[40] Fourier inversion yields the three-dimensional definite integral $\int F(x,y,z)dxdydz$ of the scattering potential, extended over the illuminated volume. No structural information will be obtained in this case. At present all OCT techniques use backscattering at $\theta=-\pi$ and a wavelength range from, say, λ_1 to λ_2. These techniques give access to a set of Fourier data on the $\mathbf{K}_z$-axis. Hence from Fourier theory the two-dimensional definite integral $\int F(x,y,z)dxdy$ of the scattering potential is obtained, yielding an average over the illuminated area in the x-y plane with spatial resolution in the z direction.

In addition, it can be seen that backscattering as used in LCI and OCT gives access to only high spatial frequencies, i.e., discontinuities, in the scattering potential. With a wavelength range from λ_1 to λ_2 we obtain Fourier components in the scattering potential within the spatial frequency range $[K_1, K_2]=[4\pi/\lambda_1, 4\pi/\lambda_2]$. With a superluminescent diode (SLD) at a wavelength of λ=800 nm and a wavelength range of $\Delta\lambda=\pm 10$ nm, we have $[K_1,K_2]=[0.0157\ \text{nm}^{-1}, 0.016\ \text{nm}^{-1}]$ or spatial (optical) period lengths of the order of magnitude of λ (which does not necessarily correspond to the resolution that might actually be available). Nevertheless, only relatively abrupt changes in the scattering potential, occurring within a few wavelengths, can be seen by backscattering tomography.

Finally let us consider the direction of the scattering vector $\mathbf{K}$. From Eq. (4) it follows, that the scattered field is determined by waves with amplitudes proportional to Fourier components of the three-dimensional scattering potential $F(\mathbf{r})$ of the form $\exp(-i\cdot\mathbf{K}\cdot\mathbf{r})$. For illustration, let us split $\exp(-i\cdot\mathbf{K}\cdot\mathbf{r})$ into cosine and sine parts. The cosine component $\cos(\mathbf{K}\cdot\mathbf{r})$ represents a cosinusoidal distribution (of the scattering potential) in space with $\mathbf{K}$ as its normal vector, i.e., as a vector normal to planes $\mathbf{K}\cdot\mathbf{r}$ =constant. The additional sinusoidal components allow for the possibility of adjusting the spatial phases properly.[40] Hence the scattering experiment yields a decomposition of the scattering potential into a three-dimensional spectrum of harmonics that are constant in planes normal to $\mathbf{K}$. Hence backscattering light gives access to only those harmonics in the spatial Fourier spectrum of the scattering potential which have their plane normals oriented more or less parallel to the direction of illumination.

The above results correspond to an alternative theoretical analysis performed recently by Pan et al.[41] These authors show by means of Monte Carlo simulations that in turbid tissue OCT detects the local variations in path length-resolved reflectance.

3 LOW COHERENCE INTERFEROMETRY

LCI or ''interference with white light''[42] has been used for many years in industrial metrology, e.g., to measure the thickness of thin films,[43] as a position sensor,[44] and with other measurands that can be

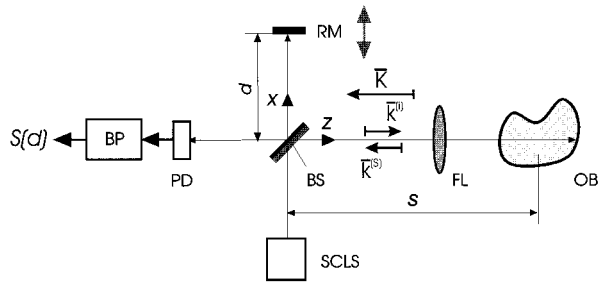

Fig. 4 Partial coherence Michelson (two-beam) interferometer. SCLS, short coherence length light source; BS, beam splitter; RM, reference mirror, terminating the reference beam; FL, focusing lens, focuses the measurement beam onto the object; OB, object illuminated by the measurement beam; PD, photodetector; BP, band pass; $S(d)$, electronic interferometer signal.

converted to a displacement.[45] At present all OCT techniques use LCI to obtain depth information. Though diffraction tomography would be the more or less natural tomographic technique,[4] it is not used at present because of the large amount of data that would have to be recorded and processed. So far only (one-dimensional) length measurements have been performed with this technique.[11] At present all OCT techniques rely on conventional LCI. Nevertheless, below we use a one-dimensional version of Wolf's[6] solution for diffraction tomography to obtain an analytical description of the light wave backscattered from the object. In the subsequent one-dimensional analysis, it is more convenient to use a convolution formulation to solve the scattering process. This can be directly derived from Eq. (4), which can also be expressed as a convolution of the scattering potential with the scattering function $\exp(i\mathbf{Kr})$:

$$
\begin{aligned}
&E^{(s)}(\mathbf{r},\mathbf{k}^{(s)},t)\\
&\quad=-\frac{A^{(i)}\cdot\exp(-i\cdot\omega\cdot t)}{4\cdot\pi\cdot D}\cdot\exp(i\cdot\mathbf{k}^{(i)}\cdot\mathbf{r})\int_{V(\mathbf{r}')}F(\mathbf{r}')\\
&\qquad\cdot\exp(-i\cdot(\mathbf{k}^{(s)}-\mathbf{k}^{(i)})\cdot\mathbf{r}')\\
&\qquad\cdot\exp[i\cdot(\mathbf{k}^{(s)}-\mathbf{k}^{(i)})\cdot\mathbf{r}]\cdot d^3\mathbf{r}'\\
&\quad=-\frac{A^{(i)}\cdot\exp(-i\cdot\omega\cdot t)}{4\cdot\pi\cdot D}\cdot\exp(i\cdot\mathbf{k}^{(i)}\cdot\mathbf{r})\int_{V(\mathbf{r}')}F(\mathbf{r}')\\
&\qquad\cdot\exp(-i\cdot\mathbf{K}\cdot(\mathbf{r}-\mathbf{r}'))\cdot d^3\mathbf{r}'\\
&\quad=-\frac{A^{(i)}\cdot\exp(-i\cdot\omega\cdot t)}{4\cdot\pi\cdot D}\cdot\exp(i\cdot\mathbf{k}^{(i)}\cdot\mathbf{r})\\
&\qquad\cdot F(\mathbf{r})\otimes\exp(i\mathbf{Kr}).
\end{aligned}
\tag{5}
$$

Let us consider the low coherence interferometer depicted in Fig. 4. The two interferometer arms are assumed to be illuminated by light waves

$$E(z,k,t)=A^{(i)}\exp(ikz-i\omega t)$$

and

$$E(x,k,t)=A^{(i)}\exp(ikx-i\omega t),$$

respectively with the same intensities $I^{(i)}=\frac{1}{2}\epsilon_0 cn|A^{(i)}|^2$ at the beam splitter BS at $x=z=0$. Hence we have two waves, each returning from one arm of the interferometer:

First there is the reference wave E_R reflected at the reference mirror at $x=d$ with the scattering potential $\delta(x-d)$:

$$
\begin{aligned}
E_R(x,k,t)&=-\frac{A^{(i)}}{4\pi}\exp(ikx-i\omega t)\cdot\exp(-iKx)\\
&\quad\otimes\delta(x-d)\\
&=-\frac{A^{(i)}}{4\pi}\exp[-ik(x-2d)-i\omega t]\\
&=E[-(x-2d),k,t].
\end{aligned}
\tag{6}
$$

This wave is reflected as a collimated wave; hence we have omitted the attenuating factor D in the denominator of the scattered amplitude. As this beam is reflected at the beam splitter toward the (negative) z axis, from here on we replace the x argument in E_R by z:

$$E_R(z,k,t)=E(-(z-2d),k,t).$$

Second, at the beam splitter we have the object wave backscattered by the scattering potential of the object:

$$
\begin{aligned}
E_0(z,k,t)&=-\frac{A^{(i)}}{4\pi s}\exp(ikz-i\omega t)\int F(z')\\
&\quad\cdot\exp[-iK(z-z')\cdot dz']\\
&=E(-z,k,t)\otimes F(z).
\end{aligned}
$$

In the denominator of the scattered amplitude we have used a mean distance s (cf. Fig. 4) of the object from the beam splitter.

These two waves interfere on their way back after passing the beam splitter. The intensity then is (we omit some constant factors)[46]:

$$I(d,k)=\langle|E_R+E_0|^2\rangle=I_R+I_0+2\mathrm{Re}\{\langle E_R{*}\cdot E_0\rangle\}.$$

Behind the beam splitter the two waves propagate colinearly along the negative z axis. Hence we have

$$
\begin{aligned}
\langle E_R{*}\cdot E_0\rangle&=\langle E{*}[-(z-2d),k,t]\cdot E(-z,k,t)\otimes F(z)\rangle\\
&=\langle E{*}[-(z-2d),k,t]\cdot E(-z,k,t)\rangle\otimes F(z);
\end{aligned}
$$

$\langle\cdots\rangle$ is the ensemble average over the product of two wave fields with unit amplitude delayed by

$$\tau=\frac{2d}{c}.$$

This ensemble average depends only on the time delay between the two waves, i.e., on the (time) coherence $g^{(1)}(\tau)$ of the light used:

$$\langle E_R^* \cdot E_0 \rangle = \frac{A^{(i)2}}{16\pi^2 s} g^{(1)}\left(\frac{2d}{c}\right) \otimes F(d). \quad (7)$$

Hence at reference mirror position $z=d$, the interference term equals the real part of the convolution of the scattering potential $F(z)$ with the coherence function $g^{(1)}(\tau)$ of the light used:

$$I(d) = I_R + I_0 + 2 \cdot \mathrm{Re}\{\langle |E_R + E_0|^2 \rangle\}$$
$$= I_R + I_0 + \frac{A^{(i)2}}{8\pi^2 s} \mathrm{Re}\left\{ g^{(1)}\left(\frac{2d}{c}\right) \otimes F(d) \right\}, \quad (8)$$

i.e., the coherence function obviously plays the role of a point spread function (PSF).

Most of the light sources used in OCT at present do have a Gaussian frequency spectrum. Hence they also have a Gaussian degree of first-order coherence[46]

$$g^{(1)}(\tau) = \exp(-i\omega_0\tau - \tfrac{1}{2}\delta^2\tau^2), \quad (9)$$

where $\tau_c = 2[2 \cdot \ln 2]^{1/2}/\delta$ is the FWHM value of $g^{(1)}(\tau)$ or coherence time (δ is the half width at 60.65% of the maximum of the Gaussian frequency spectrum and $\Delta\omega$ is the FWHM value), and $c \cdot \tau_c = l_c$ is the coherence length of Gaussian frequency light:

$$l_c = \frac{4 \cdot \ln 2}{\pi} \cdot \frac{\lambda^2}{\Delta\lambda}, \quad (10)$$

$\Delta\lambda$ is the corresponding spectral wavelength width. (If the coherence time is defined as $\Delta t = \int_{-\infty}^{+\infty} |g^{(1)}(\tau)|^2 \cdot d\tau$,[47] we have $l_c = 1.3 \cdot c \cdot \Delta t$.)

The intensity at the photodetector at the interferometer exit is

$$I(d) = I_R + I_0 + \frac{A^{(i)2}}{8\pi^2 s}$$
$$\cdot \mathrm{Re}\left\{ \exp\left[-i\omega_0 \frac{2d}{c} - \frac{1}{2}\delta^2 \left(\frac{2d}{c}\right)^2 \right] \otimes F(d) \right\}$$
$$= I_R + I_0 + \frac{A^{(i)2}}{8\pi^2 s} \cdot \cos\left(\omega_0 \frac{2d}{c}\right)$$
$$\cdot \exp\left[-\left(\frac{4 \cdot \ln 2 \cdot d}{l_c}\right)^2 \right] \otimes F(d), \quad (11)$$

i.e., the longitudinal PSF is $\exp\{-11.1 \cdot [(d-z)/l_c]^2\}$ with a FWHM of $l_c/2$.

Besides the time delay considered above, the wave may also experience scattering and absorption on its way to and from the backscattering site in the object. Whereas absorption only attenuates the amplitude, scattering introduces waves with additional path differences and thus will reduce the coherence of the backscattered wave.

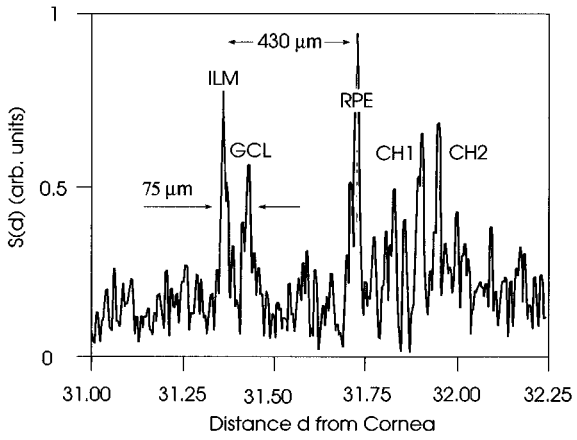

Fig. 5 LCI signal obtained with the dual-beam technique at the papilla at 10 deg nasal and 2 deg superior (λ=852 nm; l_c=30 μm in tissue). The signal peaks are ILM, inner limiting membrane; GCL, ganglion cell layer or interface between nerve fiber layer and GCL; RPE, retinal pigment epithelium (Bruch's membrane); CH1 and CH2, choroid layers (Sattler, Haller).

3.1 NOISE

One of the main noise sources in interferometry is mechanical $1/f$ noise. To achieve shot-noise-limited detection, a heterodyne technique can be used. The most straightforward realization in optics is to use the Doppler effect, e.g., by simply moving the reference mirror with constant speed v. Then we have $d = v \cdot t$ and the interference term of $I(d)$ is time modulated by $I(t) = I_R + I_o + \sqrt{I_R \cdot I_o}\cos[2\omega_0(v/c)t)]$. The corresponding photodetector signal is bandpass filtered with the Doppler frequency $2\omega_0 v/c$ as the center frequency, then rectified and low-pass filtered. The output of the low-pass filter is the envelope $S(d)$ of the oscillating part of $I(d)$ from Eq. (11):

$$S(d) = \exp\left[-11.1 \cdot \left(\frac{d}{\tau_c c}\right)^2 \right] \otimes F(d)$$
$$= \int \exp\left[-11.1 \cdot \left(\frac{d-z}{l_c}\right)^2 \right] \cdot F(z) \cdot dz. \quad (12)$$

Hence the electronic interferometer signal $S(d)$ equals the scattering potential convolved with the envelope of the real part of the coherence function. (Figure 5 shows an example of an interferometric signal $S(d)$ obtained at the fundus of a human eye *in vivo*.)

In addition to $1/f$ noise, there are several other noise sources such as quantum noise, shot noise, and electronic noise.[48] The impact of these disturbances on the measurement can be described by the signal-to-noise ratio (SNR), which is the ratio of the expected mean photocurrent power to its standard deviation. The dynamic range *DR* of an instrument

is defined by the ratio of the maximum to the minimum measurable photocurrent power P of the interferometer signal S:

$$DR = 10 \cdot \log \frac{P_{\max}}{P_{\min}} = 10 \cdot \log(SNR_{\max}).$$

Photocurrent P power is proportional to the square of the light intensity impinging at the photodetector; hence $P_{\max}/P_{\min}=R^2_{\max}/\ R^2_{\min}=1/R^2_{\min}$ and we have

$$DR = -20 \cdot \log(R_{\min}),$$

where $R_{\min}$ is the minimal reflectivity in the object beam producing a photodetector signal power equal to the standard deviation of the photocurrent power generated by a reflectivity of $R_{\max}=1$. In case of LCI and OCT, the intensity at the photodetector is caused by the interference of the object beam with the reference beam. Hence according to the interference law, the signal intensity at the photodetector is proportional to the square root of the object intensity and we have in this case

$$DR = -10 \cdot \log(R_{\min}).$$

Dynamic ranges of 90 to 140 dB were reported[49,50] when using the reflectometer technique, whereas 57 dB were reported for the original dual-beam technique.[51] The main reasons for the smaller *DR* reported so far for the original dual-beam technique are different definitions.[52] Moreover, the curvature of the reference wave reflected at the cornea restricts the aperture for the detection of the interferences in the dual beam technique. However, this latter restriction can easily be removed, e.g., by focusing the reference beam at the corneal surface.

3.2 RESOLUTION

In imaging optics, transversal resolution is usually defined by the Rayleigh criterion: Two object points are resolved if the center of the PSF (Airy disk) of one object point falls on the first zero of the PSF generated by the second.[53] The same is true in OCT. Longitudinal (or z-) resolution in OCT, however, depends on coherence length of the light used. As shown above, the longitudinal PSF in LCI might not have zeros. Correspondingly, we define here the minimum resolvable longitudinal separation as twice the FWHM of the longitudinal PSF. As can be seen from Eq. (12), the FWHM width of the exponential equals $l_c/2$. Hence the z resolution of LCI with *backscattered* light is $\Delta z = l_c/2$. Modern SLDs in the near-infrared range at $\lambda \cong 800$ nm have spectral bandwidths of approximately 15 nm. Using multielectrode pumping of single quantum well heterostructure SLDs, spectral bandwidths of approximately 70 nm have been achieved.[54] Assuming a Gaussian frequency spectrum, these bandwidths lead to corresponding coherence lengths in the range from 43 to 10 μm. Using fluorescence light of an Ar laser-pumped Ti-sapphire crystal, a spectral width of $\Delta\lambda=144$ nm (centered at 780 nm) has been obtained[55] with a corresponding coherence length of $l_c=4.2$ μm. Also, synthesized light sources might be used to enhance resolution. Using two multimode laser diodes with a wavelength difference of $\Delta\lambda=108$ nm (centered at $\lambda=730$ nm), an effective coherence length of $l_c=4$ μm was obtained.[45] Resolution in the range of one wavelength (and below) can be achieved if the so-called central fringe, i.e., the maximum of the intensity $I(d)$ at the photodetector can be identified. Wang et al.[56] describe a technique based on the application of two mutually incoherent sources with different central wavelengths. This technique, however, might only be useful in LCI.

3.3 SPECTRAL CHANGES AND DISPERSION

Longitudinal resolution might be impaired by spectral changes of the light emitted by the source on its path through the interferometric setup. Spectral changes of light can occur as a result of propagation,[57,58] interference,[59,60] multimode dispersion in fibers,[61] band-limited reflection and antireflection coatings of bulk optics (W. Drexler, private communication) and as a result of chromatic dispersion in fibers and/or bulk optics and in the object under measurement. Dispersion reduces fringe contrast and elongates the coherence length. The usual LCI technique locates the maximum of the coherence function to perform the measurement. Hence, resolution might be substantially reduced by dispersion.[62] However, it is possible to maintain high precision, even in case of severe dispersion: Danielson and Boisrobert[63] showed how the phase slope of the Fourier transform of the (time-domain) interferogram can be used to locate reflections arising from refractive index discontinuities with a precision of approximately 20 nm. LCI implies interference between finite wave packets or wave ''groups'' rather than interferences between monochromatic waves. Length is measured by detecting the amplitude maximum of the wave group. In a dispersive medium, the phase velocity depends on the frequency. Hence the group velocity differs from the phase velocity and to obtain geometrical distances, the optical distances from LCI measurements have to be divided by the group index of the medium.[64,65]

3.4 IMPLEMENTATION OF LCI

The most straightforward implementation of LCI would be to use the interferometer depicted in Fig. 4. In fact, a corresponding system has been used by Dresel et al.[66] for surface-profiling of industrial objects. In medicine and biology, however, the inherent mechanical instability of *in vivo* objects leads to errors in the interferometer signal. This problem can be overcome either by moving the reference mirror at high speed,[67] or by using the self-

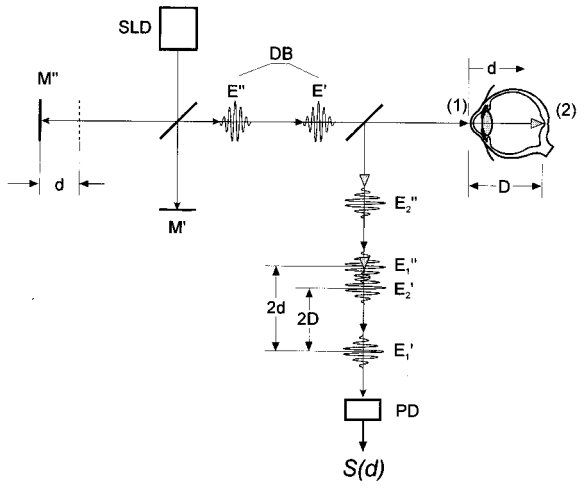

Fig. 6 Dual-beam Michelson interferometer.[52] SLD, superluminescent diode; PD, photodetector; $S(d)$, interferometer signal. The object is illuminated by a dual beam (E' and E'') generated by a Michelson interferometer. If the distance D of light-remitting sites 1 and 2 in the object is matched to the path difference d of the interferometer, interferences between corresponding beam components (E_1'' and E_2') occur. Here a translational movement of the object has no impact on the matching condition and does not generate an error in the distance measurement. Moving one of the interferometer mirrors with constant speed yields the LCI scan and a corresponding heterodyne Doppler shift.

compensating dual-beam technique.[14] Similar dual-beam interferometers for remote measurements have been described by other authors.[68–72]

The first application of LCI to ophthalmology, however, was described by Fercher and coworkers in 1986.[14] They used the dual-beam technique in a Fabry-Perot interferometer configuration and a multimode laser diode. Operating the laser at low injection current levels, a coherence length in the range of 10 μm has been obtained. No heterodyne technique was used in these early experiments. The Fabry-Perot configuration is particularly simple and easy to adjust. One problem of this interferometer is, however, that path difference zero between the two interferometer plates can hardly be obtained. Hence this technique is limited to the measurement of distances larger than, say, a few tens of micrometers and, what is more, calibration of the instrument to path difference zero is difficult to achieve. Hitzenberger has described a dual-beam Michelson interferometer using the Doppler heterodyne technique (Fig. 6).[73] He too used a multimode laser diode at λ=780 nm and a coherence length of approximately l_c=100 μm. Later[52] he used SLDs at λ=830 nm with a coherence length of approximately l_c=20 μm as light sources.

One problem of the original dual-beam technique is that the intensity of the two beam components illuminating cornea and retina cannot be adjusted independently. Sekine et al.[74] use a Mach–Zehnder configuration to achieve that separation. In addition, they use wavelength tuning of a single-mode laser diode by modulating the injection current and derive the distance to be measured from the resulting phase shift of the interference fringes. The phase shift of the interference fringes in an attached Michelson interferometer with a known path difference is used to calibrate the measurement. Because of the limited tuning range of this technique, the precision obtained was not very convincing. The use of tunable lasers with external resonators, however, could definitely improve this situation. Another modification of the dual-beam technique has been proposed by Chen et al.[75] They use the dual-beam technique together with a tilted optical flat to separate the two beam components illuminating the eye. Using a laser diode biased below its threshold ($l_c \approx 21$ μm) yielded a precision of up to 2 μm.

In 1987 Takada et al.[76] and Danielson et al.[77] described a new reflectometer for fault location in optical waveguides and fibers based on LCI. They also used a dual-beam principle. A superluminescent diode was used as a light source in a fiber optic interferometer together with a bulk-type Michelson interferometer implementing the dual-beam principle. At the same time Youngquist et al.[78] described their so-called coherence-domain reflectometry technique, which in fact is LCI. They use a partial coherence Michelson interferometer with a short-coherence length laser diode. One of the interferometer mirrors is replaced by the device under evaluation. The reference mirror translates to match the reflection site within the device. A piezoelectric transducer (PZT) attached to the reference mirror oscillates in order to generate the heterodyne frequency of the interferometer signal.

The first application of a conventional coherence domain reflectometer to ophthalmology was described by the Boston group in 1991.[17] A bulk-optics interferometer with a modified Michelson configuration was used. The light source was a laser diode (center wavelength λ=818 nm) with antireflection coatings on both facets to convert it into a SLD. The reference mirror was mounted on a computer-controlled translation stage. Heterodyne operation was achieved with a PZT transducer vibrating the reference mirror and lock-in detection of the interferometer signal. A resolution of 10 μm was obtained with that instrument.

Clivaz and co-workers[79] also used a fiber-optic Michelson interferometer and an edge-emitting diode (LED) at λ=1300 nm with a bandwidth of $\Delta\lambda$=60 nm and a corresponding resolution of 14 μm in air. They used lock-in detection with piezoelectric fiber stretching phase modulation. Later[80] they improved the spatial resolution dramatically by using fluorescent light of a Ti-sapphire crystal pumped by an Ar laser. An extremely broad spectrum of $\Delta\lambda$=144 nm was obtained at λ=780 nm, yielding a spatial resolution of 1.5 μm in tissue.

Several papers from the Boston group describe further modifications of the reflectometer technique. For example, a high-speed fiber optic Mich-

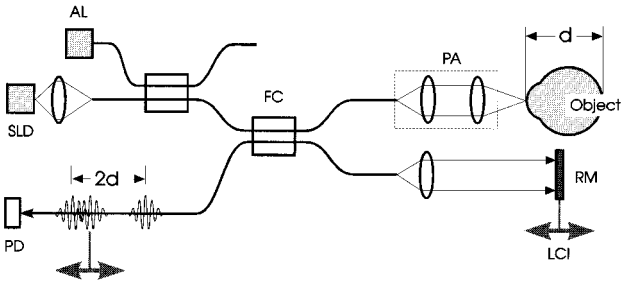

Fig. 7 Fiber optic high-speed Doppler reflectometer applied in ophthalmology (adapted from Swanson[50]). AL, aiming laser; SLD, superluminescent diode; FC, fiber coupler, PA, probe arm; PD, photodetector; RM, reference mirror; LCI (double arrow), reference mirror shift (and corresponding reference signal shift in LCI). Note: An axial movement of the object with respect to the reference mirror position during the measurement leads to a corresponding error in the measured position of the light-reflecting site in the object.

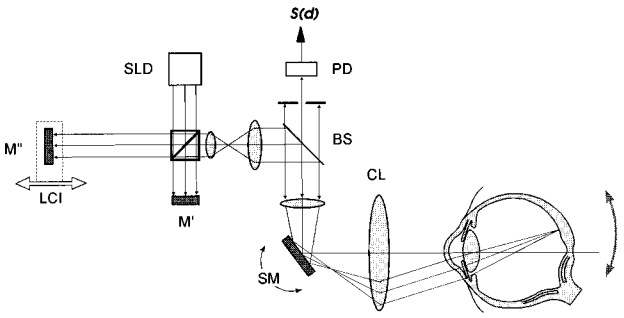

Fig. 8 Simple sector scan of the eye's fundus with the dual beam technique. At each fundus position the reference mirror *M*″ scans (open double arrow) a distance corresponding to the depth of the tomogram. SLD, superluminescent diode; *M*′, *M*″, Michelson interferometer mirrors; BS, beam splitter, SM, scanning mirror; CL, condenser lens; PD, photodetector.

elson Doppler interferometer with a SLD as light source was described by Swanson et al. (Figure 7)[50] The FWHM value of the power spectrum was 17.4 nm and a resolution of approximately 17 μm had been achieved. A fiber optic heterodyne Michelson interferometer with a titanium-sapphire laser at λ=830 nm and piezoelectric fiber optic phase modulation has been used by Hee et al. in transillumination tomography.[81,82] Here the temporal discrimination of the femtosecond technique is improved by simultaneously using coherent heterodyne detection.

An interesting new implementation of LCI was put forward by Plissi et al.[83] They describe a twin Mach–Zehnder interferometer. Here a sensing interferometer used to perform the measurement has a preset optical path difference whereas the reference interferometer matches the path difference within the coherence length. The interesting feature here is that the reference interferometer is implemented as an integrated optics configuration in lithium niobate. One of the arms of the interferometer can be scanned by the electro-optic effect.

4 OPTICAL COHERENCE TOMOGRAPHY

As already mentioned, the most straightforward technique for obtaining tomographic images would be to use diffraction tomography. The object would be illuminated by a light beam and from the measured scattered field data, the three-dimensional distribution of the scattering potential $F(r)$ would be computed and used to computationally generate two-dimensional tomographic images of any orientation. There are, however, two constraints that hinder the implementation of three-dimensional diffraction tomography. First of all, the inversion of the scattered field data is satisfactorily solved only in case of weakly scattering objects. Second, the amount of scattered field data needed to obtain a true high-resolution three-dimensional reconstruction of the object is so large that currently available light sources and scanning devices would lead to unacceptably large data acquisition times. Hence at present all OCT schemes are straight ray scanning beam schemes that obtain the depth information by LCI. The measured two-dimensional LCI signal data set is converted to gray scale or false-color images, usually on a logarithmic scale. Basically, as in diagnostic ultrasound, simple sector scan (Figure 8), simple linear scan (Figure 9), and compound scan are possible.

A first step toward tomography is the generation of topograms. Figure 10 shows the first topogram of the human fundus obtained with dual beam LCI, presented at the ICO-15 SAT conference in 1990.[84,64]

The first application of LCI to obtain tomographic images was described in 1991 by Huang et al.[12] A fiber-optic Michelson interferometer with an SLD operating at λ = 830 nm and a coherence length of 34 μm was used as a light source (Fig. 9). Heterodyne operation was achieved by a combination of Doppler shift together with piezoelectric phase

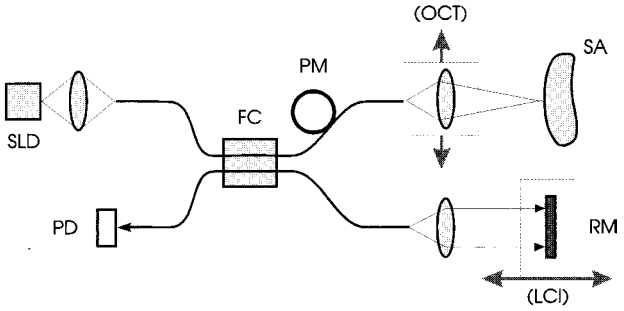

Fig. 9 Scheme of the first OCT scanner (adapted from Huang et al.[12]) based on the reflectometer technique. SLD, superluminescent diode; FC, fiber coupler; PM, piezoelectric phase modulator; SA, sample; RM, reference mirror; PD, photodetector; LCI (double arrow), LCI scan; OCT (double arrow), lateral scanning of the probe beam.

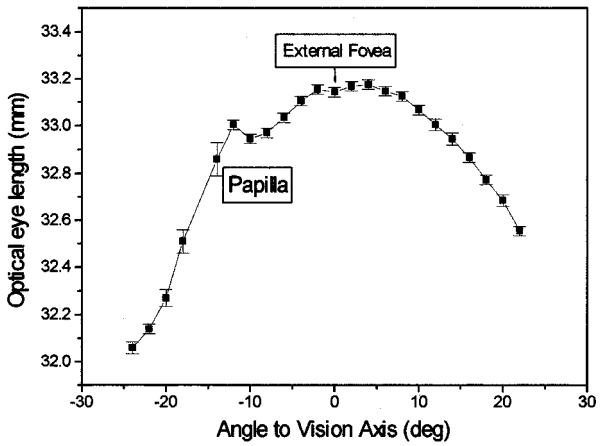

Fig. 10 First topographic surface profile of the pigment epithelium (or Bruch's membrane) of a human eye *in vivo* obtained by LCI. Note that the external fovea can be seen, hence the corresponding LCI signal is caused by Bruch's membrane or a closely associated interface.

modulation and frequency filtering of the photodetector signal. The longitudinal LCI scan was performed by high-speed continuous motion of the reference mirror of the Michelson interferometer. Tomographic images were synthesized from a series of LCI signals obtained from beam positions translated laterally between the LCI scans.

The first *in vivo* tomogram was obtained with the dual-beam LCI technique.[13] In this first implementation, the dual beam illuminating the eye was fixed and the eye was rotated with the help of a fixation beam illuminating the fellow eye. In the same year the Boston group presented *in vivo* tomograms obtained with the reflectometer LCI technique.[20] In both techniques the tomographic image has to be synthesized from linear LCI scan data. Usual image processing techniques can be used to interpolate adjacent image data. When acquiring *in vivo* data from patients with the reflectometer, motion artifacts occur from involuntary rotational and translational eye movements. These artifacts from translations can be compensated, at least partially, by cross-correlating interferometer signals obtained from adjacent LCI scans. The dual-beam technique, however, is not sensitive to translational movements of the eye.

5 RESULTS

OCT and LCI have found applications in industrial metrology as well as in medical imaging. These applications include such different fields as optical characterization of materials, characterization of fluid velocity, microscopy in scattering media, femtosecond transillumination tomography, and measurement of surface profiles. At present, however, the generation of tomographic images in ophthalmology is by far the most important application of OCT. OCT has been shown to be a powerful tool in imaging of macular diseases, in high-resolution imaging of the anterior eye, in retinal imaging, and in the quantification of the thickness of nerve fiber layers. Using light with a large spectral width not only yields short coherence lengths but also gives access to the spectral dependence of the measured figures. The correlation of optical properties with the physiologic function of a tissue is expected to provide relevant diagnostic information.

5.1 LCI

The interferometer signal $S(d)$ is dependent on several object parameters such as optical layer thickness, spatial distribution of the refractive index, scattering coefficient, birefringence, and absorption coefficient, and on the transmittance of the interferometer. Hence besides the geometrical parameters such as the positions of scattering potential discontinuities, LCI also gives access to optical properties of biological tissue and thus enables differentiation of tissue infrastructure.

5.1.1 Measurement of Optical Properties of Tissues

Most of the results mentioned above were obtained on more or less transparent tissues. LCI can also be used to measure distances and parameters in turbid media. The first use of LCI to measure parameters of diffusing multiple-scattering tissue was made by Clivaz et al.[79] The structure of the wall of postmortem bovine superior mesenteric arteries has been analyzed using an LED at λ=1300 nm. From the LCI signal, the refraction index of the intima surface, the thickness of the arterial wall, and the total transmission coefficient could be evaluated. Later, authors from the same group[80] reported on high-resolution LCI measurements using an Ar laser-pumped Ti-sapphire crystal at λ = 780 nm. The (geometrical) thickness of the cornea of fresh postmortem excised pig eyes was measured with a precision of ± 2.3 μm. In spite of the high resolution obtained with this device, no internal structure of the cornea was seen. In another experiment, measurements on the arterial wall of bovine superior mesenteric arteries have been repeated with this interferometer. Now, due to the high resolution of the instrument, details of the structure of the intima have become clearly visible.

A very thorough study on the measurement of optical properties of biological tissue by LCI was performed by Schmidt et al.[85] Using a commercially available reflectometer operating at λ=1300 nm layer thickness, backscattering coefficients and attenuation coefficients of *in vivo* dermis from three locations on a human subject and a variety of excised animal tissues were obtained. The single-mode fiber through which the light was emitted and captured was placed in direct contact with the sample. A curve-fitting method for media consisting of homogeneous layers has been developed. It

is based on a single backscattering approximation, taking into account attenuation along the path of the wave before and after it is backscattered. For example, the epidermis appeared to be thickest in the finger, followed by the forearm, the thinnest in the lip. The total attenuation coefficient of the dermis was found to be approximately 4 or 5 mm^{-1} on the finger and forearm with relatively small variations whereas the dermis on the lips was significantly less optically dense.

Characterization of optical fibers is an important task in various fields. Wang et al.[86] report on the application of LCI to the characterization of human scalp hairs using a fiber optic interferometer with an SLD at λ=850 nm. Cross-sectional scans normal to the hair axis reflect the three distinct hair layers: the outermost portion or cuticle, the cortex, and the medulla. Because the cortex is the densest portion of the shaft, light is assumed to propagate primarily through this layer. Hence longitudinal LCI scans were used to estimate the refractive index of the cortical region. Regardless of shaft color, the refractive index of the cortical region turned out to be within the range from 1.56 to 1.59.

LCI has also been shown to yield birefringence information. Attenuation and birefringence of the tunica media in a calf coronary artery has been measured using a low-coherence reflectometer.[87] Combining this information with measurements of layer thickness may enable noninvasive identification and evaluation of the thickness of retinal nerve fibers thermally damaged versus normal tissue, and arterial plaque versus normal arterial wall.

A new technique that demonstrates how light propagates in diffusely scattering materials has been described recently by G. Häusler et al.[88] A Mach–Zehnder interferometer with one of the mirrors replaced by the sample is used. The sample is illuminated by the one interferometer beam and the scattered light is observed perpendicularly to the axis of illumination via the second interferometer arm. Using LCI techniques, it is possible to visualize those photons which have traveled the same path length. Hence the spatial distribution of absorption and scattering and the scattering anisotropy coefficient can be measured with this technique.

5.1.2 LCI in Ophthalmology: Intraocular Distances

The eye is an optical instrument. Its performance relies on several parameters such as axial length, chamber depth, optical power of cornea and lens, and others to remain stable within narrow limits. One of the more important applications of intraocular distance biometry at present is the axial eye length (AEL) measurement for cataract surgery. The problem here is to predict the converging power of that artificial lens that would produce emmetropia. The precision of the standard ultrasonic technique is limited to 0.1 mm at most, but 0.2 mm are more realistic. The remaining error of 0.2 to 0.3 mm in the axial length, however, causes a residual error of 1 diopter in the outcome of the surgery procedure and the patient would have to use corrective glasses. Other important geometrical parameters in ophthalmology are the corneal thickness (CT), anterior chamber depth (ACD), lens thickness (LT), retinal thickness, and the thickness of single retinal layers.

AEL measurements were evaluated in a realistic situation.[89] A total of 196 cataract eyes were measured using dual-beam LCI and two different ultrasonic techniques. The performance of dual-beam LCI was evaluated as a function of cataract grade and compared with the ultrasonic techniques. The optical technique yielded systematically longer eye lengths than ultrasound. More than 90% of the cataract eyes were measurable using a prototype dual-beam LCI instrument. A precision of 20 μm was obtained independently of the cataract grade. Problems occurred only with very dense cataract lenses and with patients suffering from heavy tremor or other fixation problems because of the rather slowly working prototype interferometer.[89] CT profiles were measured on 18 eyes ranging from 20 deg nasal to 25 deg temporal. The precision was $\pm$1.6 μm for central measurements and decreased to $\pm$3.5 μm at the large angles.[52] This result is considerably better than that of conventional optical pachometers or ultrasound pachometers. In addition, no significant interobserver variability was observed. In ACD and LT measurements, a precision of $\pm$10 μm was obtained.[90] Preliminary accommodation studies revealed a decreasing ACD and an increasing LT with decreasing focus distance.

The interferometer signal from the fundus shows several peaks (see Fig. 5). At the moment, only the identity of the peaks from the internal limiting membrane and from the retinal pigment epithelium (RPE) respectively from Bruch's membrane seem warranted because of the structure of their topograms (see, e.g., Fig. 10). There is, however, good evidence (see results) that the distance between the first two larger peaks (ILM and GCL in Fig. 5) correlates with the nerve fiber layer thickness even though the association of the GCL peak with the ganglion cell layer is speculative. On this basis, the thickness of retinal layers was measured with a precision of $\pm$5 μm.[51]

5.2 OCT

OCT uses LCI to generate two-dimensional images of internal structures of biological tissues or other objects. Multiple LCI scans are performed at a series of laterally adjacent positions analogous to ultrasound B-mode imaging. Low-coherence reflectometry[12] and dual beam LCI[13] have been used.

5.2.1 Metrologic Applications of OCT

Tearney et al.[91] used OCT to determine the refractive index of human tissue *in vitro* and *in vivo*. In the first method, the refractive index was computed from the optical thickness of the tissue as obtained from an OCT image. In the second method, OCT was used to measure noninvasively the refractive index by focus tracking when moving the sample in an axial direction. *In vitro* and *in vivo* refractive indices of human skin, muscle, and adipose tissue were measured with a standard deviation on the order of 0.01. Optical Doppler tomography was used by Wang et al.[49] to determine the velocity profiles of fluid flows *in vitro* with a modified reflectometer. The fluid velocity was obtained from the power spectra of the Doppler-shifted interferometer signal. In these experiments, a relative velocity uncertainty of 7% was obtained.

5.2.2 OCT in Imaging

OCT has furthermore been used to improve existing imaging procedures. For example, OCT was used to enhance optical sectioning in confocal microscopy.[92] By fixing the reference arm length of the low coherence interferometer and transverse scanning, high-contrast transversal slice images of an object embedded in a scattering medium were obtained. This technique is particularly promising if the light distribution in the image plane is dominated by light scattered from other planes. OCT has also been used to improve the femtosecond transillumination technique.[81] Here time gating is improved by coherent heterodyne detection of ballistic photons. Submillimeter resolution was obtained in images of absorbing objects in media of 27 mean-free-scattering path thicknesses. If ballistic photons are absent, the early-arriving coherent portion can also be detected using LCI heterodyne detection.[82]

Schmidt et al.[93] describe the application of LCI in a Mach–Zehnder interferometer to image-absorbing structures in a random medium. Here too, the temporal discrimination property of LCI is used to preferentially detect ballistic photons transmitted through a random medium. A dramatic dependence of the optical thickness through which images can be transmitted on the coherence length of the light used has been found.

In their first paper on OCT, the Boston group described the (*in vitro*) application of OCT to the examination of the coronary arterial wall. Normal arterial wall could be distinguished from atherosclerotic plaque.[17] A first experimental step toward the application of OCT in dermatology was carried out by Brunner et al.[94] Several techniques to overcome the intensity problems caused by weak signals from internal structures of turbid objects were described in that study.

5.2.3 OCT in Ophthalmology

The diagnostic potential of OCT for noncontact biometry and identification of abnormalities of the anterior segment of the eye was demonstrated by Izatt et al.[19] Using the reflectometer technique at λ=830 nm (and l_c=14 μm in air), structures such as the cornea, sclera, iris, and lens anterior capsule were clearly visible. High spatial frequency sampling resulted in the visualization of the corneal epithelium, the stroma, and the endothelium (see Figure 11—color plate). Biometric data were obtained from the anterior chamber depth, the anterior chamber angle, the radii of curvature of the cornea, the corneal refraction power, the corneal thickness, and the thickness of the epithelial layer. Also the first qualitative images from an *in vitro* study on bovine eyes toward cataract grading were reported.

Many retinal diseases are accompanied by changes in retinal thickness. Hence high depth resolution is an important feature of any imaging technique used to diagnose retinal pathology. Current diagnostic instruments such as the confocal scanning laser ophthalmoscope are limited to a depth resolution not better than 300 μm.[95] Against this background, high-resolution OCT is an extremely promising new diagnostic technique. The potential of OCT in diagnostic imaging of macular diseases was assessed by Puliafito et al.[22] Fifty-one eyes were examined in a recent study using light from an SLD at λ=830 nm, yielding a depth resolution of 10 μm and a transversal resolution of 13 μm in the retina. Large-scale anatomical features such as the fovea, optic disk, and retinal profile could easily be identified by their characteristic morphological features. Retinal thickening caused by macular edema and other diseases could be estimated quantitatively. Pathologies such as full thickness macular hole (Figure 12—color plate), lamellar macular hole, epiretinal membrane, cystoid macular edema, central vein occlusion, retinal detachment, and the result of photocoagulation treatment were correlated with fundus examination and fluorescein angiography. OCT images of serous retinal pigment epithelium and pigment epithelial detachment demonstrated the accumulation of optically clear fluid in the subretinal and sub-RPE spaces. A comparison of tomograms of serous neurosensory detachments showing a highly reflective band with RPE detachments that displayed a thin, highly backscattering layer just beneath the neurosensory retina confirmed that the RPE and choriocapillaris normally appear together as a highly backscattering layer in the OCT images used here. Further studies[23,24] demonstrated the potential of OCT to quantify the amount of serous retinal detachments, macular holes, and macular edema.

Quantitative measurements of the retinal thickness and its layers are of particular importance in the assessment of glaucoma. Using the reflectome-

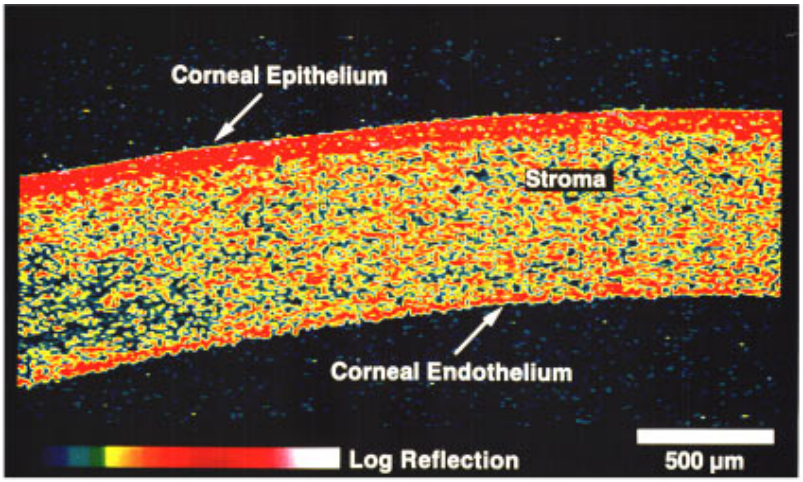

Fig. 11 High-resolution OCT of the cornea (courtesy of J. A. Izatt et al.[19]); the image is displayed in false color, where bright colors (red to white) correspond to high scattering potential, and dim colors (blue to black) correspond to low scattering potential.

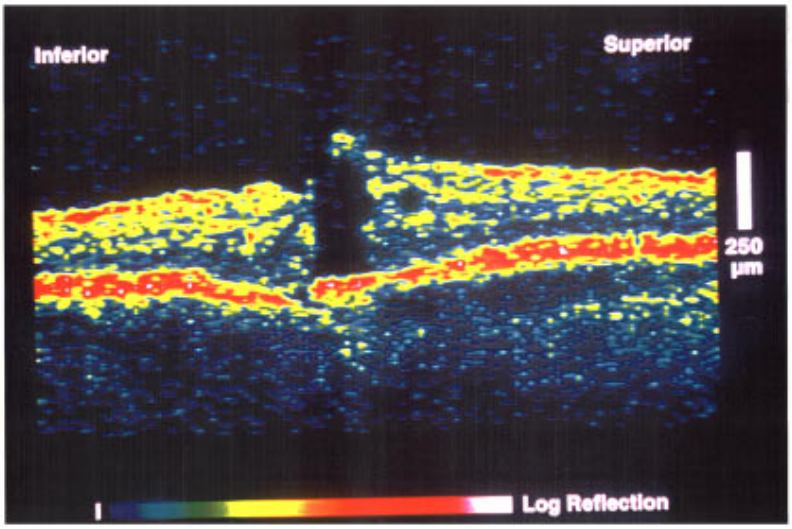

Fig. 12 Full thickness macular hole, including the neurosensory layer, terminating just above the highly reflective band of RPE and choriocapillaris and an associated operculum at the internal limiting membrane at the border to the low scattering dark vitreous humor above (courtesy of C. A. Puliafito et al.[22]).

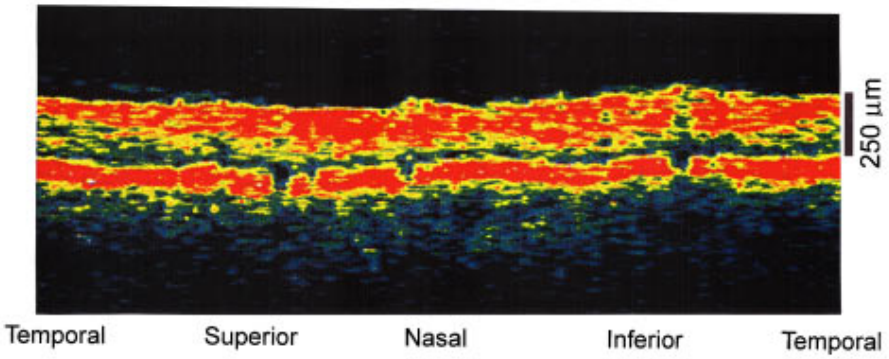

Fig. 14 Optical coherence tomography of a normal eye taken in a cylindrical section of tissue concentric with the optic nerve head, with a scan diameter of 3.37 mm. False color image as in Figs. 11 and 12. The anteriormost (on top) red reflection is interpreted as nerve fiber layer. The red reflection on the bottom is the RPE together with choroid and sclera. The nerve fiber layer thickens superiorly and inferiorly. (Courtesy of J. S. Schuman et al.[25]).

COLOR PLATE

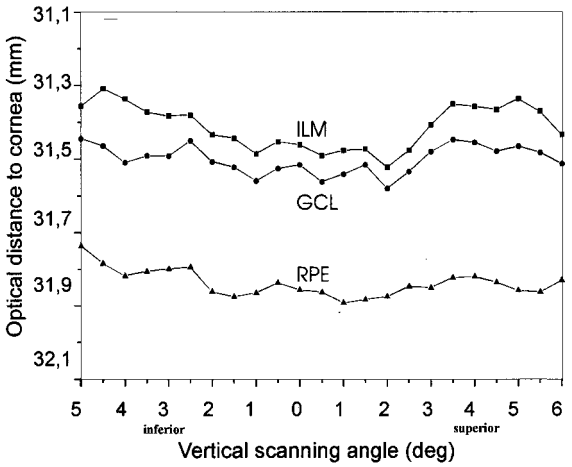

Fig. 13 Topographic presentation of interfaces of retinal layers of a normal eye.[51] Vertical retinal section across the papilla slightly nasal from the center at 14 deg nasal from 5 deg inferior to 6 deg superior. The optical thickness of the retina ranges between 345 and 520 μm; the optical thickness of the nerve fiber layer ranges between 42 and 175 μm. Geometrical distances can be obtained by dividing the optical distances by the group index of the corresponding eye media (approx. 1.4). ILM, inner limiting membrane; GCL, ganglion cell layer; RPE, retinal pigment epithelium.

ter technique, Hee et al.[21] demonstrated the application of OCT to high-resolution imaging of the normal human retina. A fiber optic reflectometer with an SLD operating at λ = 843 nm and an FWHM-coherence length of 10 μm in the eye was used. The RPE and choriocapillaris were delineated by a highly reflective band. The retinal thickness, measured from the vitreoretinal interface to the RPE and choriocapillaris, varied from 310 μm at the margin of the fovea to 130 μm at its center. Another highly backscattering band adjacent to the vitreoretinal interface could be associated with the retinal nerve fiber layer (RNFL). In a 1.5-disk diameter circular tomogram centered at the optic disk, the NFL thickness varied between 40 and 230 μm.

Similar results were obtained by Drexler et al.[51] These authors used the dual-beam LCI technique. By deriving the borders of retinal layers directly from the LCI signals, topograms of retinal interfaces were obtained (Figure 13). A superluminescent diode, Superlum SLD-361 (λ=832 nm; $\Delta\lambda$=27 nm; l_c=26 μm) was used. The maximum (geometrical) NFL thickness at a slightly nasal location was 125 μm and the minimum thickness was 45 μm. The (geometrical) retinal thickness ranged from 250 to 370 μm. The standard deviation of repeated measurements at the same retinal location was 5 μm.

A pilot study on the quantification of NFL thickness in normal and glaucomatous eyes was conducted by Schuman et al.[25] A total of 59 eyes of 33 subjects were studied using, besides conventional ophthalmologic examination, the reflectometer technique with an SLD operating at λ=843 nm and an FWHM-coherence length of 10 μm in the eye

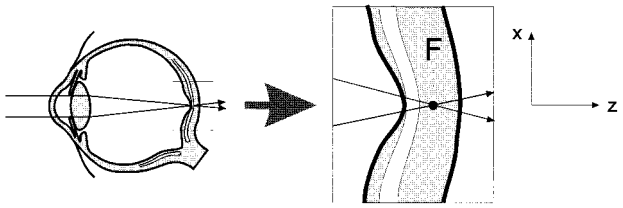

Fig. 15 Transversal (x-) resolution in ophthalmologic OCT. Because of the limited depth of focus, optimal transversal resolution at the fundus of the eye is obtained only at the focus F of the illuminating beam.

(see Figure 14—color plate). The depth resolution was also 10 μm. As Tuulonen et al.[96] have shown in a clinical study that a decrease in NFL thickness precedes the onset of glaucomatous field loss by up to 6 years, one might expect OCT to dramatically improve glaucoma diagnosis because of its unsurpassed depth resolution. (In NFL thickness measurements with confocal scanning laser ophthalmoscopy, e.g., the variability is larger than 100 μm.) In the pilot study mentioned, NFL thickness measured by OCT also demonstrated a higher degree of correlation with the functional status of the optic nerve than cupping or neuroretinal rim area. Visual field defects were strongly related to thinner NFL. Finally, a decrease of NFL thickness with aging was found.

6 RECENT AND POSSIBLE FUTURE DEVELOPMENTS

6.1 HIGH-RESOLUTION OCT USING A DYNAMIC COHERENT FOCUS (DCF)

One of the problems of the now established OCT techniques is that transversal resolution depends on the position of the beam focus within the object. To attain equal x-y resolution throughout the whole object depth during the LCI scan, the focus of the measurement beam has to be moved synchronously with the reference mirror, e.g., by shifting the focusing lens FL in Fig. 4 synchronously with the reference mirror RM (see Figure 15). If the optical path in the reference beam equals the optical path in the measurement beam with the focus as end point, optimal transversal resolution will be maintained throughout the depth of the whole object.

When using OCT in ophthalmology, however, this technique cannot readily be used, because the focusing lens is the eye's optics. Here the concept of the dynamic coherent focus can be used. In this technique, a focus is created that remains coherent to the reference beam during the whole scanning procedure. The LCI scan is then performed by shifting the coherent focus throughout the object depth. The basic principle is depicted in Figure 16.

Here the reference mirror RM is fixed. The measurement beam is first directed toward the focusing lens FL and then focused into the beam focus BF

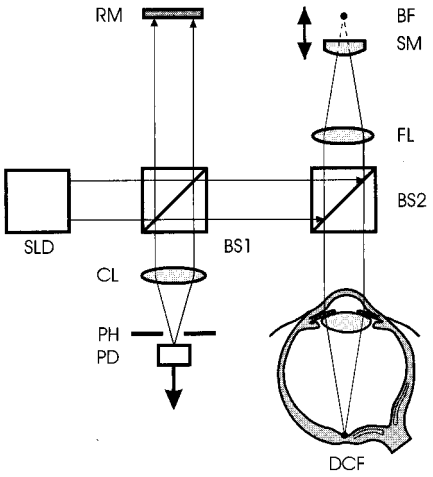

Fig. 16 Dynamic coherent focus (DCF) interferometer. SLD, superluminescent diode; BS1, BS2, beam splitter; RM, reference mirror; FL, focusing lens; SM, spherical scanning mirror performing the LCI scan; BF, beam focus; DCF, dynamic coherent focus; CL, collimating lens; PH, pinhole, PD, photodetector.

coinciding with the center of curvature of the spherical scanning mirror SM. The reflected beam is recollimated by the focusing lens FL and the optics of the eye forms the dynamic coherent focus DCF at the fundus of the eye. If the focal length of FL equals the focal length of the eye, the dynamic coherent focus DCF will be shifted by the same amount along the optical axis as the beam focus BF. The backscattered light is again reflected toward the scanning mirror SM and from there toward the photodetector via the two beam splitters. If the optical length of the reference beam matches the optical length in the measurement beam with the dynamic coherent focus as end point, then this will be maintained even if the dynamic focus DCF scans the object. Hence optimal transversal resolution throughout the whole scanning depth is obtained.

6.2 SPECTRAL OCT BY SPECTRAL INTERFEROMETRY (SI)

The use of a spectrometer to evaluate the spectral modulation of light remitted from an object illuminated by spatially coherent light in order to measure distances of internal light remitting structures was described by the author in 1991.[97] This technique can be combined with spectroscopy. Spectroscopy has become an important tool in medical diagnosis and pathology.[98] Near-infrared spectroscopy allows noninvasive monitoring of cerebral oxygenation.[99] Visible light pulse oximetry has already been used to measure arterial oxygen saturation from spectrally resolved reflectance at the retinal fundus.[95] Schweitzer et al.[101] obtained reflection spectra of fundus vessels and their neighborhood with high spatial and spectral resolution using a fundus camera together with a spectrograph. Because Beer's law includes the path length of the light-absorbing structure, a more thorough technique would have to take into account the distance travelled by the light through the tissue. This could be provided by LCI or OCT. Using wavelength tuning interferometry (see below) and SI techniques,[11] spectral and depth information could be obtained at once.[102,103]

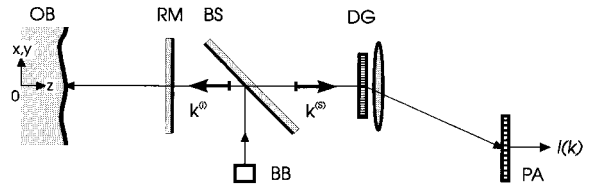

Fig. 17 Spectral interferometry technique using a broadband light source (e.g., a SLD) and a spectrometer. BB, broadband light source; BS, beam splitter; RM, reference mirror; OB, object, DG, spectrometer diffraction grating; PA, photodiode array.

In the analysis of Sec. 2 it was shown that light of a wide range of wavenumbers k has to be used in order to obtain access to the three-dimensional object structure. This can be performed by either LCI or by spectral techniques. In the spectral techniques, either a "white" or broadband light source can be used together with a spectrometer, as indicated in Figure 17 (SI technique) or a tunable laser can be used as in the wavelength tuning technique (WTI technique) indicated in Figure 18. Usually SI uses broadband light sources emitting light with a wide range of wavenumbers like SLDs. Then a spectrometer is needed to display the intensity of the remitted light at the various wavelengths (or wavenumbers).

Here the spectral distribution of the scattered light $I(k)$ is measured with the help of a grating spectrometer and the object structure is obtained via an inverse Fourier transform of $I(k)$. The first length measurements on a stack of cover glasses[104] as well as on a model eye and thickness measurements of the cornea of a human eye *in vivo* have been published.[11,103] A similar technique is being

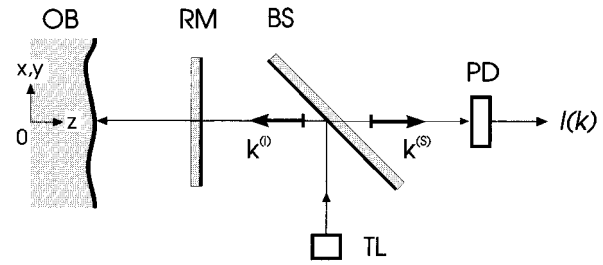

Fig. 18 Wavelength tuning interferometer with a tunable laser (TL). BS, beam splitter; RM, reference mirror; OB, object; PD, photodetector.

used to measure the scattering amplitude in tissue phantoms.[105]

6.3 SPECTRAL OCT BY WAVELENGTH TUNING INTERFEROMETRY

In the WTI technique, the wavelength of the light used is tuned over a range of wavenumbers k and the spectral light intensity $I(k)$ remitted from the object is detected by a photodetector. From $I(k)$ the scattered field is obtained and an inverse Fourier transform yields the distribution of the scattering potential along the illuminating beam. Additional implications of this technique have been discussed in a recent publication.[11] This technique seems rather promising since external cavity tunable lasers with wavelength tuning ranges up to 70 nm in the 800-nm range might become commercially available.[106]

Wavelength tuning was used in the past by Sekine et al.[74] These authors used the wavelength shift of a laser diode on a pulse-modulation drive. Length was measured by relating the phase differences caused by the wavelength shift in the measurement interferometer to those obtained from a reference interferometer with a known path difference.

Another tuning scheme that might be used in the future is based on the chirp technique, well known from radar. Here too the frequency of the light emitted is periodically varied, e.g., in a sawtoothed fashion.[107] This leads to an additional narrowing of the corresponding degree of coherence and it may be possible to achieve a further shortening of the coherence length beyond the limit given by the usual frequency bandwidth/time duration limit.[108] In addition, hopping between discrete wavelengths, e.g., mode hopping and ''channel hopping,'' which have been used in the past to measure length,[109,110] might be used to further shorten the coherence length and thus improve longitudinal resolution.

6.4 ODT (OPTICAL DOPPLER TOMOGRAPHY)

Recently LCI has been combined with the Doppler technique to measure flow velocities at precisely defined spatial locations.[49] Spatial profiles of fluid flow velocities in transparent glass and turbid collagen conduits were measured with a local resolution of approximately 5 μm and a velocity uncertainty of 7%.

7 CONCLUSION

OCT is an exciting, new, high-resolution imaging technique. Transversal and longitudinal resolution in the micrometer-range and dynamic ranges up to 140 dB have been obtained so far. OCT shows an extremely high potential as a noninvasive diagnostic tool in ophthalmology. Future developments might include new fields of application such as dermatology and include additional information like Doppler shift, birefringence, and tissue spectrometric data.

Acknowledgment

The author thanks members of the Boston OCT group for some of their tomographic images and his colleagues at the Institute of Medical Physics of the University of Vienna for numerous contributions. Part of this work is based on results of projects financed by the Austrian Science Foundation (FWF projects P10316-MED and P9781-MED).

REFERENCES

1. J. Radon, ''Über die Bestimmung von Funktionen durch ihre Integralwerte laengs gewisser Mannigfaltigkeiten,'' *Ber. Verh. Saechs. Akad. Wiss. Leipzig Math Phys.* **69**, 262–277. (1917).
2. S. Webb, *The Physics of Medical Imaging*,'' Adam Hilger, Bristol and Philadelphia (1988).
3. G. Müller, et al., *Medical Optical Tomography: Functional Imaging and Monitoring*, SPIE, Bellingham, WA (1993).
4. A. C. Kak and M. Slaney, *Principles of Computerized Tomographic Imaging*, IEEE Press, New York (1988).
5. H. P. Baltes, ed., *Inverse Source Problems in Optics*, Springer-Verlag, Berlin (1978).
6. E. Wolf, ''Three-dimensional structure determination of semi-transparent objects from holographic data,'' *Opt. Commun.* **1**, 153–156 (1969).
7. E. Wolf, ''On the fundamental theorem of diffraction tomography,'' Proc. SPIE **1983**, 618–619 (1993).
8. M. Kartal, B. Yazgan, and O. K. Ersoy, ''Multistage parallel algorithm for diffraction tomography,'' *Appl. Opt.* **34**, 1426–1431 (1995).
9. W. H. Carter and P.-C. Ho, ''Reconstruction of inhomogeneous scattering objects from holograms,'' *Appl. Opt.* **13**, 162–172 (1974).
10. A. F. Fercher, H. Bartelt, E. Becker, and H. Wiltschko, ''Image formation by inversion of scattered field data: experiments and computational simulation,'' *Appl. Opt.* **18**, 2427–2439 (1979).
11. A. F. Fercher, C. K. Hitzenberger, G. Kamp, S. Y. El-Zaiat, ''Measurement of intraocular distances by backscattering spectral interferometry,'' *Opt. Commun.* **117**, 43–48 (1995).
12. D. Huang, E. A. Swanson, C. P. Lin, J. S. Schuman, W. G. Stinson, W. Chang, M. R. Hee, T. Flotte, K. Gregory, C. A. Puliafito, and J. G. Fujimoto, ''Optical coherence tomography,'' *Science* **254**, 1178–1181 (1991).
13. A. F. Fercher, C. K. Hitzenberger, W. Drexler, G. Kamp, and H. Sattmann,'' In Vivo optical coherence tomography,'' *Am. J. Ophthalmol.* **116**, 113–114 (1993).
14. A. F. Fercher and E. Roth, ''Ophthalmic laser interferometry,'' *Proc. SPIE* **658**, 48–51 (1986).
15. A. F. Fercher, K. Mengedoht, and W. Werner, ''Eye length measurement by interferometry with partially coherent light,'' *Optics Lett.* **13**, 186–188 (1988).
16. World Service International, ''Getting the eye's measure with lasers,'' *Photonics Spectra* **24**, No. 3, 90–91 (1990).
17. D. Huang, J. Wang, C. P. Lin, C. A. Puliafito, and J. G. Fujimoto, ''Micron-resolution ranging of cornea anterior chamber by optical reflectometry,'' *Lasers Surg. Med.* **11**, 419–425 (1991).
18. J. A. Izatt, M. R. Hee, D. Huang, J. G. Fujimoto, E. A. Swanson, C. P. Lin, J. S. Shuman, and C. A. Puliafito, ''Ophthalmic diagnostics using optical coherence tomography,'' *Proc. SPIE* **1877**, 136–144 (1993).
19. J. A. Izatt, M. R. Hee, E. A. Swanson, C. P. Lin, D. Huang, J. S. Schuman, C. A. Puliafito, and J. G. Fujimoto, ''Micrometer-scale resolution imaging of the anterior eye in vivo with optical coherence tomography,'' *Arch. Ophthalmol.* **112**, 1584–1589 (1994).
20. E. A. Swanson, J. A. Izatt, M. R. Hee, D. Huang, C. P. Lin, J.

S. Shuman, C. A. Puliafito, and J. G. Fujimoto, ''In vivo retinal imaging using optical coherence tomography,'' *Opt. Lett.* **18**, 1864–1866 (1993).
21. M. R. Hee, J. A. Izatt, E. A. Swanson, D. Huang, J. S. Schuman, C. P. Lin, C. A. Puliafito, and J. G. Fujimoto, ''Optical coherence tomography of the human retina,'' *Arch. Ophthalmol.* **113**, 325–332 (1995).
22. C. A. Puliafito, M. R. Hee, C. P. Lin, E. Reichel, J. S. Schuman, J. S. Duker, J. A. Izatt, E. A. Swanson, and J. G. Fujimoto, ''Imaging of macular diseases with optical coherence tomography,'' *Ophthalmology* **102**, 217–229 (1995).
23. M. R. Hee, C. A. Puliafito, C. Wong, E. Reichel, J. S. Duker, J. S. Schuman, E. A. Swanson, and J. G. Fujimoto, ''Optical coherence tomography of central serous chorioretinopathy,'' *Am. J. Ophthalmol.* **120**, 65–74 (1995).
24. M. R. Hee, C. A. Puliafito, C. Wong, E. Reichel, J. S. Duker, J. S. Schuman, E. A. Swanson, and J. G. Fujimoto, ''Optical coherence tomography of macular holes,'' *Ophthalmology* **102**, 748–756 (1995).
25. J. S. Schuman, M. R. Hee, C. A. Puliafito, C. Wong, T. Pedut-Kloizman, C. P. Lin, E. Hertzmark, J. A. Izatt, E. A. Swanson, and J. G. Fujimoto, ''Quantification of nerve fiber layer thickness in normal and glaucomatous eyes using optical coherence tomography,'' *Arch. Ophthamol.* **113**, 586–596 (1995).
26. J. M. Krauss and C. A. Puliafito, ''Lasers in ophthalmology,'' *Lasers Surg. Med.* **17**, 102–159 (1995).
27. M. Born, *Optik*, 3rd ed. Springer Verlag, Berlin (1972).
28. R. Barer, ''Phase contrast and interference microscopy in cytology,'' in Physical Techniques in Biological Research, Vol. 3, G. Oster and A. W. Pollister, eds., Academic Press, New York (1956).
29. H. G. Davies, ''The determination of mass and concentration by microscope interferometry,'' in *General Cytochemial Methods*, Vol. 1, J. F. Danielli, ed., Academic Press, New York (1958).
30. K. F. A. Ross, ''The immersion refractometry of living cells by phase contrast and interference microscopy,'' in General Cytochemical Methods, Vol. 2, J. F. Danielli, ed., Academic Press, New York (1961).
31. W.-F. Cheong, S. A. Prahl, and A. J. Welch, ''A review of optical properties of biological tissues,'' *IEEE J. Quant.* **26**, 2199–2185 (1990).
32. F. P. Bolin, L. E. Preuss, R. C. Taylor, and R. J. Ference, ''Refractive index of some mammalian tissues using a fiber optic cladding method,'' *Appl. Opt.* **28**, 2297 (1989).
33. M. C. W. Campbell, ''Measurement of refractive index in an intact crystalline lens,'' *Vision Res.* **24**, 409–415 (1984).
34. G. Simonson, E. Kleberger, and H. J. Plöhn, ''Die Verteilung des Brechungsindex in der Augenlinse,'' *Optik* **29**, 81–86 (1969).
35. G. Freytag, ''Vergleichende Untersuchungen über die Brechungsindizes der Linse und der flüssigen Augenmedien des Menschen und höherer Tiere in verschiedenen Lebensaltern,'' Thesis. Wiesbaden (1907).
36. X. Clivaz, R. P. Marquis-Weible, R. P. Salathe, R. P. Novak, and H. H. Gilgen, ''High-resolution reflectometry in biological tissues,'' *Opt. Lett.* **17**, 4–6 (1992).
37. E. H. Roth, ''In vivo-Messung der Brechungsindex-Verteilung der menschlichen Linse mit Hilf der Scheimpflug-Fotografie und mit einem Helium-Neon-Laser-Strahl.'' Thesis, Düsseldorf (1989).
38. J. M. Cowley, Diffraction Physics, North Holland, Amsterdam (1975).
39. D. Dändliker and K. Weiss, ''Reconstruction of the three-dimensional refractive index from scattered waves,'' Opt. Commun. **1**, 323–328 (1970).
40. R. Bracewell, *The Fourier Transform and Its Applications*, McGraw-Hill, New York (1965).
41. Y. Pan, R. Birngruber, J. Rosperich, and R. Engelhardt, ''Low-coherence optical tomography in turbid tissue: theoretical analysis,'' *Appl. Opt.* **34**, 6564–6574 (1995).
42. P. Hariharan, *Optical Interferometry*,'' Academic Press, Australia (1985).
43. P. A. Flourney, ''White-light interferometric thickness gauge,'' *Appl. Opt.* **11**, (1972).
44. T. Li, A. Wang, K. Murphy, and R. Claus, ''White-light scanning fiber Michelson interferometer for absolute position-distance measurement,'' *Opt. Lett.* **20**, 785–787 (1995).
45. Y. J. Rao, Y. N. Ning, and D. A. Jackson, ''Synthesized source for white-light sensing system,'' *Opt. Lett.* **18**, 462–464 (1993).
46. R. Loudon, *The Quantum Theory of Light*, Clarendon Press, Oxford (1985).
47. J. W. Goodman, *Statistical Optics*, Wiley, New York (1985).
48. X. Clivaz, ''High resolution optical low coherence reflectometry in biological tissues,'' Thesis. Lausanne, EPFL (1994).
49. X. J. Wang, T. E. Milner, and J. S. Nelson, ''Characterization of fluid flow velocity by optical Doppler tomography,'' *Opt. Lett.* **20**, 1337–1339 (1995).
50. E. A. Swanson, D. Huang, M. R. Hee, J. G. Fujimoto, C. P. Lin, and C. A. Puliafito, ''High-speed optical coherence domain reflectometry,'' *Opt. Lett.* **17**, 151–153 (1992).
51. W. Drexler, C. K. Hitzenberger, H. Sattmann, and A. F. Fercher, ''Measurement of the thickness of fundus layers by partial coherence tomography,'' *Opt. Eng.* **34**, 701–710 (1995).
52. C. K. Hitzenberger, ''Measurement of corneal thickness by low-coherence interferometry,'' *Appl. Opt.* **31**, 6637–6642 (1992).
53. J. W. Goodman, *Introduction to Fourier Optics*, McGraw-Hill, New York (1969).
54. A. T. Semenov, V. K. Batovrin, I. A. Garmash, V. R. Shidlovsky, M. V. Shramenko, and S. D. Yakubovich,'' (GaAl)As SQW superluminescent diodes with extremely low coherence length,'' *Electron Lett.* **31**, 314–315 (1995).
55. X. Clivaz, F. Marquis-Weible, and R.-P. Salathe, ''1.5 μm resolution optical low coherence reflectometry in biological tissues,'' Proc. SPIE **2083**, 338–346 (1993).
56. D. N. Wang, Y. N. Ning, K. T. V. Grattan, A. W. Palmer, and K. Weir, ''Characteristics of synthesized light sources for white-light interferometric systems,'' *Opt. Lett.* **18**, 1884–1886 (1993).
57. W. H. Carter, ''A study of the propagation of optical spectra using a wavelength independent formulation of diffraction theory and coherence theory,'' *J. Mod. Opt.* **40**, 2433–2449 (1993).
58. F. Gori and E. Wolf, ''Sources which generate fields whose spectra are invariant on propagation,'' *Opt. Commun.* **119**, 447–452 (1995).
59. F. V. James and E. Wolf, ''Spectral changes produced in Young's interference experiment,'' *Opt. Commun.* **81**, 150–154 (1991).
60. D. S. Mehta, H. C. Kandpal, K. Saxena, J. S. Vaishya, and K. C. Joshi, ''Displacement measurements from coherence-induced spectral changes in a Mach–Zehnder interferometer,'' *Opt. Commun.* **119**, 352–360 (1995).
61. J. Zavadil, T. Honc, and Ctyroky, ''Influence of optical fibers on the spectrum of transmitted light-emitting-diode radiation,'' *Appl. Opt.* **34**, 4312–4315 (1995).
62. P.-L. Francois, M. Monerie, C. Vassallo, Y. Durteste, and F. A. Alard, ''Three ways to implement interferencial techniques: Application to measurements of chromatic dispersion, birefringence, and nonlinear susceptibilities,'' *J. Lightwave Technol.* **LT-7**, 500–513 (1989).
63. B. L. Danielson and C. Y. Boisrobert, ''Absolute optical ranging using low coherence interferometry,'' *Appl. Opt.* **30**, 2975–2979 (1991).
64. C. K. Hitzenberger, ''Optical measurement of the axial eye length by laser Doppler interferometry,'' *Invest Ophthalmol. Vis. Sci.* **32**, 616–624 (1991).
65. P. de Groot, ''Chromatic dispersion effects in coherent absolute ranging,'' *Opt. Lett.* **17**, 898–900 (1992).
66. T. Dresel, G. Häusler, and H. Venzke, ''Three-dimensional sensing of rough surfaces by coherence radar,'' *Appl. Opt.* **31**, 919–925 (1992).
67. E. A. Swanson, D. Huang, M. R. Hee, J. G. Fujimoto, C. P. Lin, and C. A. Puliafito, ''High-speed optical coherence domain reflectometry,'' *Opt. Lett.* **17**, 151–153 (1992).
68. R. A. Patten, ''Michelson interferometer as a remote gauge,'' *Appl. Opt.* **12**, 2717–2721 (1971).
69. G. Beheim, ''Remote displacement measurement using a

passive interferometer with a fiber-optic link,'' *Appl. Opt.* **24**, 2335–2340 (1985).
70. J. L. Brooks, R. H. Wehtworth, R. C. Youngquist, M. Tur, B. Y. Kim, H. J. Shaw, *J. Lightwave Technol.* **LT-3**, 1062 (1985).
71. T. P. Newson, F. Farahi, J. D. C. Jones, and D. A. Jackson, ''Combined interferometric and polarimetric fibre optic temperature sensor with a short coherence length source,'' *Opt. Commun.* **68**, 161–165 (1988).
72. F. Farahi, T. P. Newson, J. D. C. Jones, and D. A. Jackson, ''Coherence multiplexing of remote fibre optic Fabry-Perot sensing system,'' *Opt. Commun.* **68**, 319–321 (1988).
73. C. K. Hitzenberger, W. Drexler, and A. F. Fercher, ''Measurement of corneal thickness by laser Doppler interferometry,'' *Invest. Ophthalmol. Vis. Sci.* **33**, 98–103 (1992).
74. A. Sekine, I. Minegishi, and H. Koizumi, ''Axial eye-length measurement by wavelength-shift interferometry,'' *J. Opt. Soc. Am. A* **10**, 1651–1655 (1993).
75. S. Chen, D. N. Wang, K. T. V. Grattan, A. W. Palmer, and G. L. Dick, ''A compact optical device for eye-length measurements,'' *IEEE Phot. Tech. Lett.* **5**, 729–731 (1993).
76. K. Takada, J. Noda, and K. Okamoto, ''Measurement of spatial distribution of mode coupling in birefringent polarization-maintaining fiber with new detection scheme,'' *Opt. Lett.* **11**, 680–682 (1986).
77. B. L. Danielson and C. D. Whittenberg, ''Guided-wave reflectometry with micrometer resolution,'' *Appl. Opt.* **26**, 2836–2842 (1987).
78. R. C. Youngquist, S. Carr, and D. E. N. Davies, ''Optical coherence-domain reflectometry: A new optical evaluation technique,'' *Opt. Lett.* **12**, 158–160 (1987).
79. X. Clivaz, F. Marquis-Weible, R. P. Salathe, R. P. Novak, and H. H. Gilgen, ''High-resolution reflectometry in biological tissues,'' *Opt. Lett.* **17**, 4–6 (1992).
80. X. Clivaz, F. Marquis-Weible, and R.-P. Salathe, ''1.5 μm resolution optical low coherence reflectometry in biological tissues,'' *Proc. SPIE* **2083**, 338–346 (1993).
81. M. R. Hee, J. A. Izatt, E. A. Swanson, and J. G. Fujimoto, ''Femtosecond transillumination tomography in thick tissues,'' *Opt. Lett.* **18**, 1107–1109 (1993).
82. M. R. Hee, J. A. Izatt, J. M. Jacobson, and J. G. Fujimoto, ''Femtosecond transillumination optical coherence tomography,'' Opt. Lett. **18**, 950–951 (1993).
83. V. Plissi, A. J. Rogers, D. J. Brassington, and M. G. F. Wilson, ''Low-coherence interferometric sensor system utilizing an integrated optics configuration,'' *Appl. Opt.* **34**, 4735–4739 (1995).
84. A. F. Fercher, ''Ophthalmic interferometry (contribution to the OWLS-I-conference 1990, Garmisch-Partenkirchen, Germany),'' in Vol. 1, G. von Bally, and S. Khanna, eds. Elsevier, Amsterdam (1993).
85. J. M. Schmitt, A. Knüttel, and R. F. Bonner, ''Measurement of optical properties of biological tissues by low-coherence reflectometry,'' *Appl. Opt.* **32**, 6032–6042 (1993).
86. X. J. Wang, T. E. Milner, R. P. Dhond, W. V. Sorin, S. A. Newton, and J. S. Nelson, ''Characterization of human scalp hairs by optical low-coherence reflectometry,'' *Opt. Lett.* **20**, 524–526 (1995).
87. M. R. Hee, D. Swanson, E. A. Huang, and J. G. Fujimoto, ''Polarization-sensitive low-coherence reflectometer for birefringence characterization and ranging,'' *J. Opt. Soc. Am.* **B9**, 903–908 (1992).
88. G. Häusler, J. M. Herrmann, R. Kummer, M. W. Lindner, ''Observation of light propagation in volume scatterers with 10-11 fold slow motion,'' submitted to Optics Letters.
89. C. K. Hitzenberger, W. Drexler, C. Dolezal, F. Skorpik, M. Juchem, A. F. Fercher, and H. D. Gnad, ''Measurement of the axial length of cataract eyes by laser Doppler interferometry,'' *Invest. Ophthalmol. Vis. Sci.* **34**, 1886–1893 (1993).
90. A. Baumgartner, C. K. Hitzenberger, W. Drexler, H. Sattmann, and F. Fercher, ''Measurement of the anterior structures of the human eye by partial coherence interferometry,'' *Proc. SPIE Lasers in Opthalmology III*, 146–151 (1995).
91. G. J. Tearney, M. E. Brezinski, J. F. Southern, B. E. Bouma, M. R. Hee, and J. G. Fujimoto, ''Determination of the refractive index of highly scattering human tissue by optical coherence tomography,'' *Opt. Lett.*, **20**, 2258–2260 (1995).
92. J. A. Izatt, M. R. Hee, G. M. Owen, E. A. Swanson, and J. G. Fujimoto, ''Optical coherence microscopy in scattering media,'' *Opt. Lett.* **19**, 590–592 (1994).
93. A. Schmidt, R. Corey, and P. Saulnier, ''Imaging through random media by use of low-coherence optical heterodyning,'' *Opt. Lett.* **20**, 404–406 (1995).
94. H. Brunner, J. Strohm, M. Hassel, and R. Steiner, ''Optical coherence tomography (OCT) of human skin with a low-scan CCD-camera,'' *Proc. SPIE* **2626**, *Photon Propagation in Tissues*.
95. K. Rohrschneider, R. O. W. Burk, F. E. Kruse, and H. E. Völcker, ''Reproducibility of the optic nerve head topography with a new laser tomographic scanning device,'' *Ophthalmol.* **101**, 1044–1049 (1994).
96. A. Tuulonen, J. Lehtola, and P. J. Airaksinen, ''Nerve fiber layer defects with normal visual fields,'' *Ophthalmol.* **100**, 587–597 (1993).
97. A. F. Fercher, C. Hitzenberger, and M. Juchem, ''Measurement of intraocular optical distances using partially coherent laser light,'' *J. Mod. Opt.* **38**, 1327–1333 (1991).
98. P. Gwynne, ''A new window on biomedicine with spectroscopy,'' *Biophotonics* **1**, 52–54 (1994).
99. P. Rolfe, Y. A. B. D. Wickramasinghe, M. S. Thorniley, F. Faris, R. Houston, Zhang Kai, K. Yamakoshi, S. O'Brien, M. Doyle, K. Plamer, and S. Spencer, ''Fetal and neonatal cerebral oxygen monitoring with NIRS: Theory and practice,'' *Early Human Dev.* **29**, 269–273 (1992).
100. J. P. de Kock, L. Tarassenko, C. J. Glynn, and A. R. Hill, ''Reflectance pulse oximetry measurements from the retinal fundus,'' *IEEE Trans. Biomed. Eng.* **40**, 817–823 (1993).
101. D. Schweitzer, L. Leistritz, M. Hammer, M. Scibor, U. Bartsch, and J. Strobel, ''Calibration-free measurement of the oxygen saturation in retinal vessels of men,'' *Proc. SPIE* **2393**, 210–218 (1995).
102. A. F. Fercher, C. K. Hitzenberger, W. Drexler, G. Kamp, I. Strasser, and H. C. Li, ''In vivo optical coherence tomography in ophthalmology,'' in *Medical Optical Tomography: Functional Imaging and Monitoring*, Vol. 1S 11, B. Chance et al., eds., SPIE, Bellingham, WA (1993).
103. A. F. Fercher, W. Drexler, C. K. Hitzenberger, and G. Kamp, ''Measurement of ocular distances by optical spectrum modulation,'' *Proc. SPIE* **2083**, 263–267 (1993).
104. N. Tan-no, T. Ichimura, T. Funaba, N. Anndo, and Y. Odagiri, ''Optical multimode frequency-domain reflectometer,'' *Opt. Lett.* **19**, 587–589 (1994).
105. G. Häusler, J. M. Herrman, M. W. Lindener, and R. Ringler, ''Optical tomography-morphological analysis of volume scatterers with the spectral radar,'' submitted for publication to Optics Letters.
106. A. Mooradian, ''External cavity tunable diode lasers,'' Pamphlet of Micracor. Inc., Acton, Mass.
107. E. M. Strzelecki, D. A. Cohen, and L. A. Coldren, ''Investigation of tunable single frequency tunable diode lasers for sensor applications,'' *J. Lightwave Technol.* **6**, 1610–1618 (1988).
108. H. J. Schmitt and V. Blazek, ''System concepts for high resolution optical tomography,'' *Laser und Optoelektronik* **27**, 43–47 (1995).
109. B. S. Glance et al., ''New advances on optical components for FDR optical networks,'' *J. Lightwave Technol.* **11**, 886 (1993).
110. A. F. Fercher, W. Werner, and U. Vry, ''Two-wavelength speckle interferometry of rough surfaces using a mode hopping diode laser,'' *Opt. Laser Eng.* **11**, 271–279 (1989).

Acknowledgment: The Publishers wish to acknowledge permission received from publishers and authors to reproduce figures used in this paper.